Particle Impingement in SRM Nozzles

Hirohide IKEDA[*], Haruhito TANNO[**],
Shin-ichiro TOKUDOME[*] and Masahiro KOHNO[*]

Abstract

The ISAS' nozzle two-phase flow computer program has recently been revised to achieve a higher accuracy in calculating thrust characteristic and behavior of particle streamlines. Alumina particles had been gathered in lots of motor firings over a wide range in scale. The particle size distribution characteristics were obtained and the resulted particle sizing equation in terms of the mass averaged particle diameter D_{43} is quite close to that employed in the improved SPP, i.e., D_{43} is a unique function of motor throat diameter. Subscale motors containing highly aluminized propellant were fired, whose nozzles were designed to have significant amount of particle impingement and then sever erosion at the exit lip. The nozzle eroded locations were used to verify the computational accuracy of impingement location prediction. It has been shown that the improved two-phase flow program can well predict the particle impingement location by assuming an appropriate particle diameter Dp_{IMP}, which is proportional to D_{43}. The proportional coefficient is rather universal.

1. Introduction.

A computer program to solve the two-phase nozzle flow is an important design methodology of optimum nozzle contours. ISAS developed such a design code ten years ago to solve the two-dimensional axisymmetric gas-particle flow by the method of characteristics, where a frozen gas is assumed and the condensed phase is treated as being particles with an unchanged size.[1] The ISAS' two-phase flow program had been quite useful to predict the motor Isp but less effective to predict the behavior of limiting particle streamline, because of the lack of experimental evidences to demonstrate complicated relaxation mechanisms between particle and gas phase.

Impingement of alumina particles on nozzle exit cone inner surface causes significant thrust loss and nozzle wall damage. In 1984, the high altitude test of upper stage motor KM-P-3 was carried out. Fig.1 shows the view of postfire nozzle exit cone, which exit lip was suffered from an excessive erosion by sever particle impingement. The measured char characteristics of CP-FRP nozzle exit cone is presented in Fig.2.

Fig. 1 View of postfire KM-P-3 nozzle exit cone.

The existing two-phase program could not anticipate this anomaly. This experience gave the chance to refine the two-phase flow program to be able to predict particle impingement location. The existing program employed simple assumptions such as the Stokes' drag law and theoretical Nu=2 to evaluate momentum and energy exchange between particle and gas phase. These expressions have recently been replaced by the more improved, semi-empirical ones applicable over a wide range of flow conditions[2].

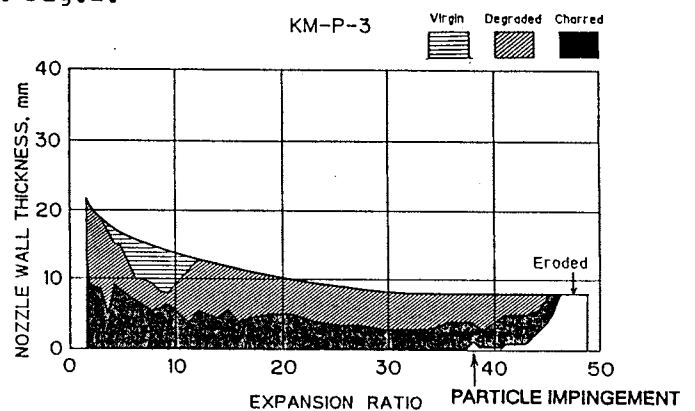
Fig. 2 Measured char characteristics of KM-P-3 nozzle exit cone.

* Institute of Space and Astronautical Science, 3-1-1 Yoshinodai, Sagamihara, Kanagawa 229, Japan
** Nissan Motor Co., Ltd. 3-5-1 Momoi, Suginami-ku, Tokyo 167, Japan

2. The characteristics of alumina particles size and distribution.

The most important variable to control the two-phase flow effects is the size of alumina particles in nozzle flow. In our analysis, alumina particles are treated as spherical and of a unique size. Alumina particles exhausted from the various size of ISAS firing test motors and launched boosters have been gathered and investigated over years. A typical photo of sampled alumina particles by scanning electron microscope is shown in Fig.3. Alumina particles are very fine and quite spherical just as reported in many other references.
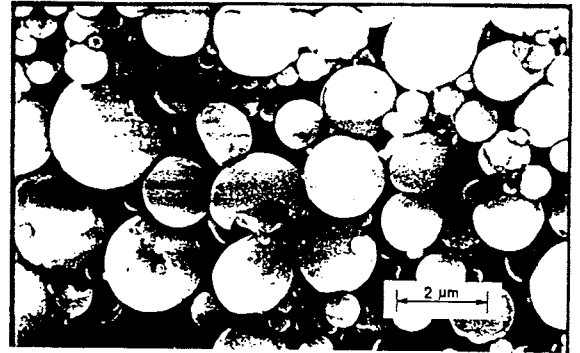
Fig. 3 Typical image of scanning electron microscope of sampled alumina particles.

A typical distribution histogram of the measured particle diameter is shown at the top of Fig.4, in terms of number and volume frequency. It is difficult to extract any feature therefrom. But when these are reduced by logarithmic formulation, as described at the bottom, number frequency distribution well follows the log-normal size distribution. It seems that there exists the maximum, upper-limited particle diameter ,which indicates that the model for particle break-up in the nozzle could be applicable[3]. The model accounts for the maximum liquid droplet size to correlate strongly with Weber number, the ratio of surface tension of droplet to shear force caused by particle velocity lags in the nozzle transonic region. Following the model, maximum stable droplet size is increased with throat diameter.

As seen at the top of Fig.5, data of mass-averaged particle diameter D_{43} are scattered around the same correlative line as that used in the improved SPP[4]. The empirical correlation is described as a function of motor throat diameter as

$$D_{43} = 1.206 \ D_t^{\ 0.293} \quad ; \ D_t : \text{throat diameter, mm}$$

Another feature is that standard deviation in log-normal distribution is almost constant 0.3 independently of throat diameter. It is to say that the shape of number frequency distribution in log form never changes by motor scale. Effects of other parameters such as chamber pressure, propellant formulation, etc. are quite negligible compared with that of throat diameter.
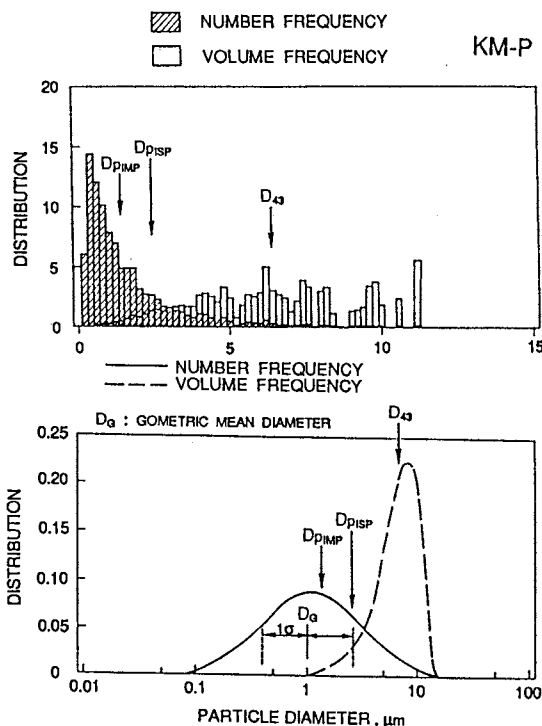
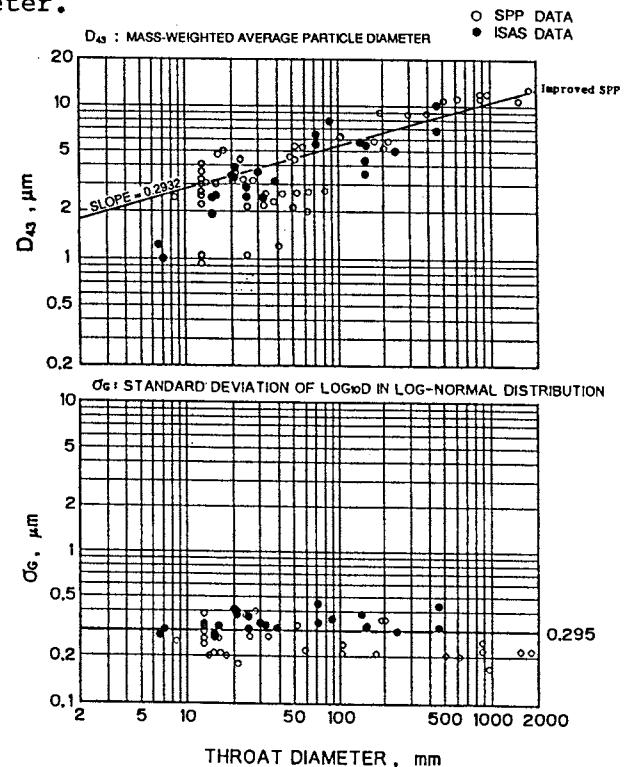Fig.4 A typical measured Alumina particle distribution.

Fig.5 Measured D43 and σ_G dependence on the motor throat diameter.

3. The prediction of Isp and particle impingement location by the improved program.

The improved ISAS' two-phase program can be used effectively for Isp prediction, only if an effective mean diameter Dp_{ISP} is assumed. The values of Dp_{ISP} were determined from the delivered Isp by using this computer code for various production motors. The resulted correlation of Dp_{ISP} on the motor throat diameter was strictly proportional to D_{43};

$$Dp_{ISP} = 0.719 \ D_t^{\ 0.293} = 0.596 \ D_{43}$$

The motor performance predictability of the improved program has already been reported in reference 5. The program can predict the motor Isp in an accuracy of $\pm 0.3\%$ by employing the particle sizing equation Dp_{ISP} both for firing test motors and for flight motors.

Particle impingement location at nozzle exit region might also be predicted by use of the revised program. The KM-P-3 nozzle eroded location was used to verify the computational accuracy of impingement location prediction. Fig.6 illustrates the KM-P-3 nozzle particle limiting streamlines by varying the mean particle diameter. And Fig.7 shows the calculated impingement location. The figure also shows the definition of the effective mean diameter Dp_{IMP} to determine the impingement location. To establish a reliable analytical method for predicting particle impingement location, more experimental evidences are required for a wide range in scale.
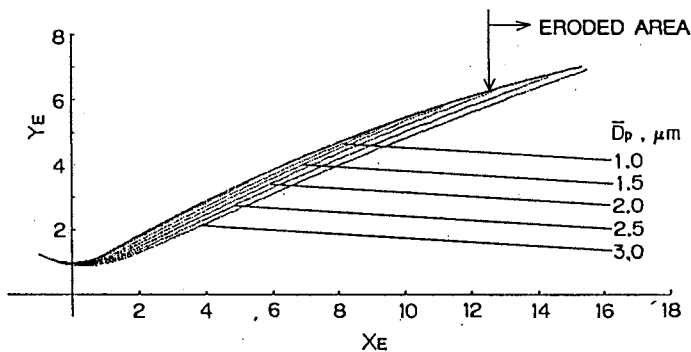

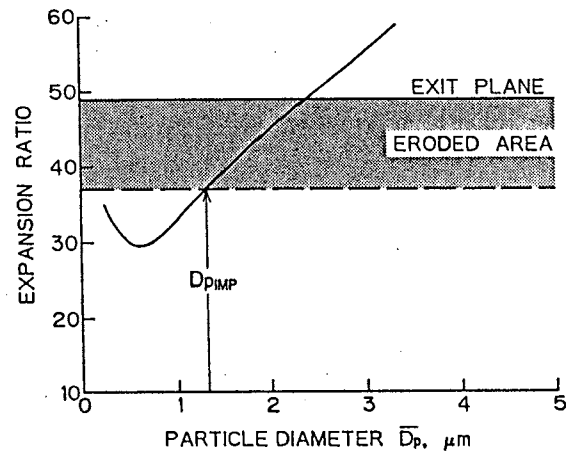Fig.6 Calculated KM-P nozzle particle limiting streamlines.

Fig.7 Calculated KM-P nozzle particle impingement location.

4. Particle impingement experiment by subscale motors.

Experimental study by small solid propellant rocket motors was carried out to obtain more data of particle impingement location. The test matrix is summarized in Table 1. Three kinds of scale motor loaded with four different types of solid propellant in practical use were fired. The throat diameter was varied from 7 to 38mm, while the exit expansion ratio was about 36 in common. Four different types of circular-arc nozzle contour were examined, all of which had longer nozzle length and higher turnback angle intentionally to cause sever particle impingement.

Table 1 Particle impingement experiment test matrix.

Run No.	Motor Signature	Propellant Propellant, Binder-%B.%Al	Mass kg	Propellant Formulation	D_t mm	ε	Circular Nozzle Type	Non-Dim. Length X_E	Initial Angle θ_B, deg.	Turnback Angle θ_{TB}, deg.	Pc MPa	Effective Burn Time s
1	TM-55 IMP-1	BP-30B	0.3	CTPB-16-16	6.6	32.6	D	17.6	30.0	30.0	5.7	2.4
2	TM-55 IMP-2	BP-106J	0.3	HTPB-14-18	7.1	32.6	D	17.6	30.0	30.0	5.3	2.3
3	TM-160 IMP-1	BP-204J	16.0	HTPB-12-20	38.0	36.0	A	16.0	29.5	24.0	5.0	4.3
4	TM-160 IMP-2	BP-30B	15.1	CTPB-16-16	30.0	36.0	A	16.0	29.5	24.0	4.5	7.4
5	TM-160 IMP-3	BP-106J	15.5	HTPB-14-18	32.0	36.0	A'	15.0	29.9	22.5	4.6	6.6
6	TM-110 IMP-11	BP-204J	3.5	HTPB-12-20	25.0	36.0	A	16.0	29.5	24.0	5.1	2.2
7	TM-110 IMP-12	BP-204J	3.5	HTPB-12-20	25.0	36.0	B	20.0	23.1	18.0	5.2	2.1
8	TM-110 IMP-13	BP-204J	3.5	HTPB-12.20	25.0	36.0	C	16.0	26.6	18.0	5.1	2.1
9	TM-110 IMP-21	BP-106J	3.4	HTPB-14-18	21.0	36.0	A	16.0	29.5	24.0	4.9	3.2
10	TM-110 IMP-22	BP-106J	3.4	HTPB-14-18	21.0	36.0	B	20.0	23.1	18.0	4.9	3.2
11	TM-110 IMP-31	BP-110J	3.4	HTPB-12-17 HMX8	20.0	36.0	A	16.0	29.5	24.0	5.5	3.1

The schematic configuration of experimental motor and nozzle is illustrated in Fig.8. Bulk graphite was used for material of the nozzle throat and exit cone so as traces of particle impact on the material surface to be observed. All the motors were fired under an altitude simulating condition by using constant area diffusers directly connected to the nozzles. Alumina particles were also gathered from the motor exhaust plume by water baths. A typical chamber pressure and test cell pressure time history is shown in Fig.9.
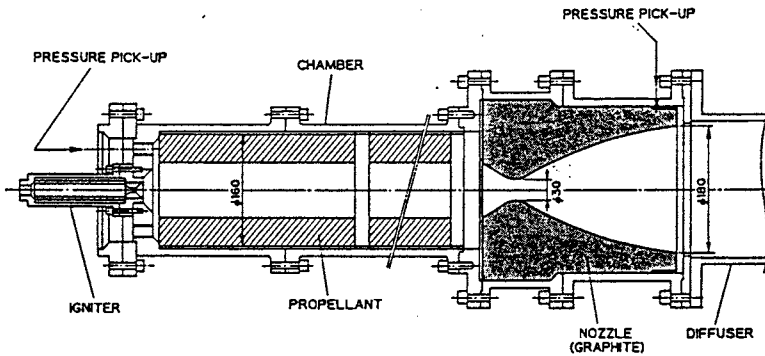
Fig. 8   Test motor and graphite
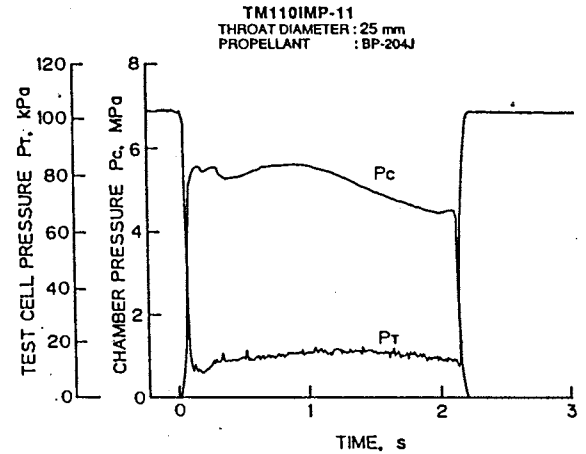   nozzle configuration.

Fig. 9   Typical pressure time traces.

Views of postfire nozzle exit cone inner surface are shown in Fig.10. There exist lots of longitudinal streaks and impinged alumina particles deposited near the nozzle exit lip. The losses of nozzle exit cone material were precisely measured by a three-dimensional linear measurement system. The obtained mechanical erosion rate characteristics along the non-dimensional nozzle length are presented in Fig.11. The particle impingement location can well be determined therefrom. The graphite erosion rate on the nozzle exit plane is enormously higher than that inserted to the throat region.[6] Particles impinging at a higher expansion ratio should have a higher kinetic energy and possibly cause more damage to the nozzle wall. These excessive erosion caused by particle impingement has never been analytically investigated as yet, because the mechanisms are very complicated by the combination of increased heat flux from combustion products and momentum exchange from massive alumina particles.
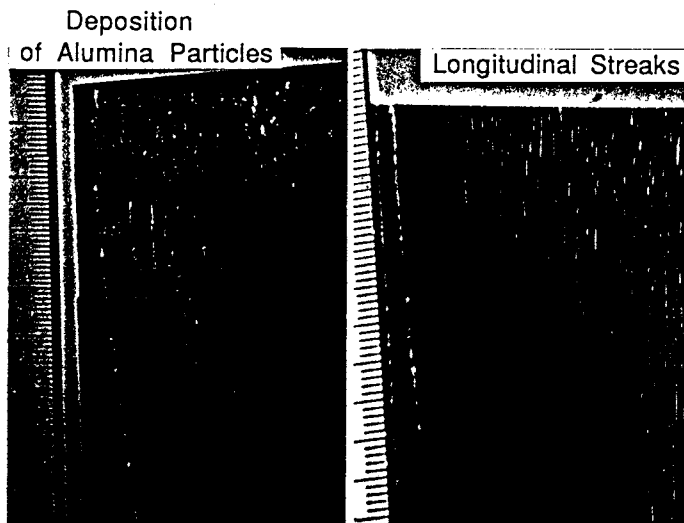
Fig. 10   Views of postfire nozzle
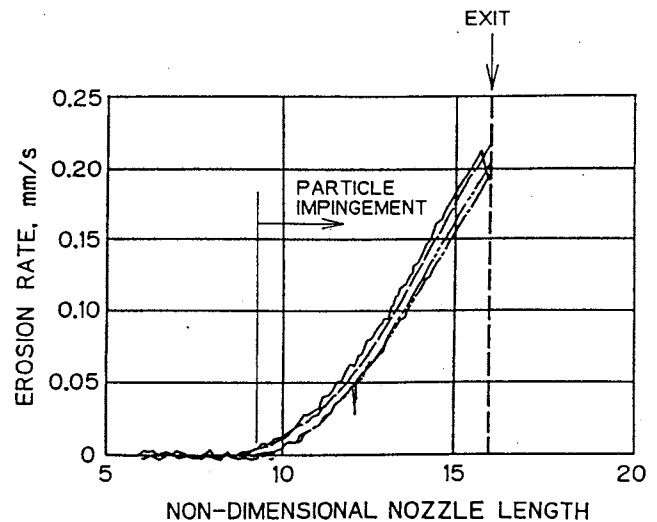   exit cone inner surface.

Fig. 11   Erosion characteristics of
          graphite nozzle exit cone.

5. Results and discussion.

The nozzle eroded locations in the test motors and the previous KM-P-3 were used to verify the computational accuracy of impingement location prediction. In Fig.12, data of the obtained particle diameter Dp_{IMP} are plotted against the motor throat diameter. It can be seen that the data are rather limited, but are well scattered around a correlative line in parallel with those for D_{43} and Dp_{ISP}. The effects of propellant formulation and nozzle contour are quite negligible compared with throat diameter within the examined range. It is concluded that Dp_{IMP} is rather small but is also a unique function of motor throat diameter.

Fig. 12 Resulted dependence of D_{43}, Dp_{ISP} and Dp_{IMP} on throat diameter.

$$Dp_{IMP} = 0.417 \ D_t^{0.293} = 0.346 \ D_{43}$$

The most important geometric parameter of contoured nozzle is the turnback angle. Turnback angle is defined as the difference between initial divergence angle just downstream of the throat and the wall angle at the exit lip. A typical contour map drawn by using the improved ISAS' program and the Dp_{ISP} and Dp_{IMP} sizing equations is presented in Fig.13, on which the design point of KM-P-3 is shown by the solid circle. The shadowed line indicates that the determined particles Dp_{IMP} impinge just at the nozzle exit lip, and the dotted domain denotes the region where impact erosion occurs. It was concluded that the excessive erosion on KM-P-3 nozzle had been resulted from its higher turnback angle. On the figure, the prohibited boundary is well correlated with the contour of turnback angle about 12 degree. Some available guidelines for nozzle contouring design avoiding particle impingement were proposed from rather empirical correlation by other investigators.[7],[8] For example, an acceptable turnback angle of 12 degree was recommended, and this correlation do not differentiate between contour types.

The schematic explanation of particle impingement on the nozzle wall is exhibited in Fig.14. The particle impingement never occurs in conical nozzle. In the contoured nozzle, initial expansion angle leads to turn the particles trajectory away from nozzle axis. When the nozzle contour turns back, the particles impinge nozzle wall because they can not turn quickly.
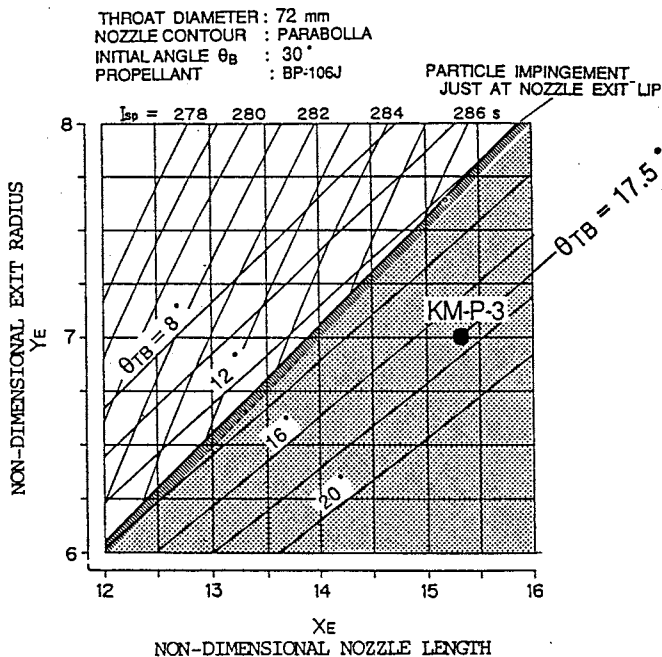

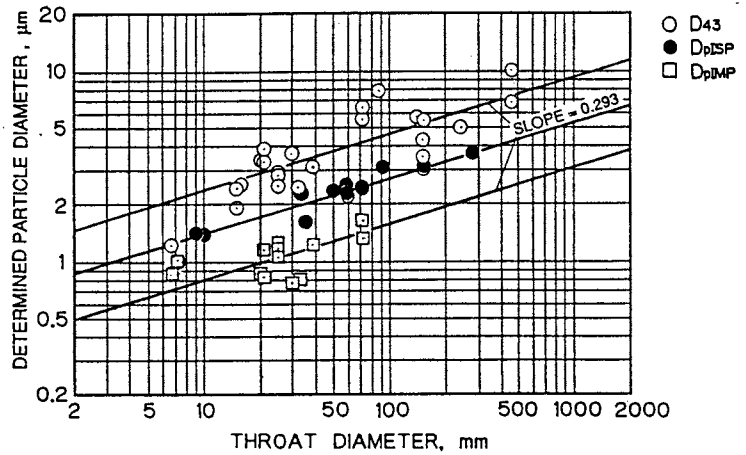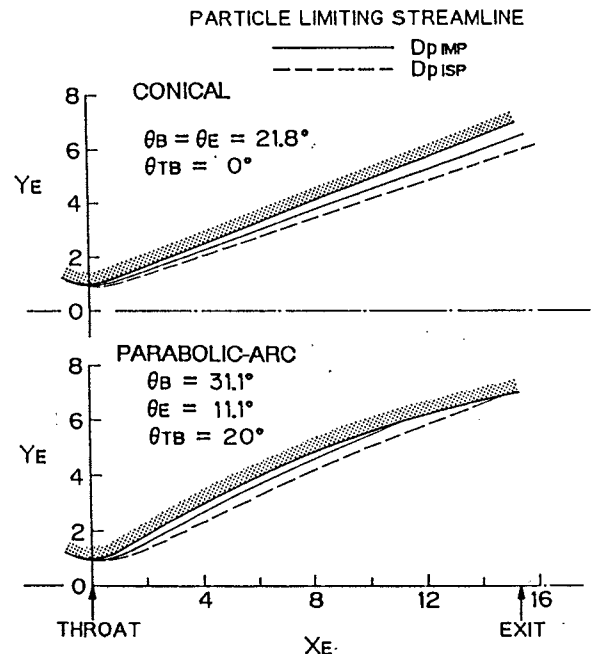Fig. 13 KM-P nozzle contour design map.

Fig. 14 Variational manner of particle limiting streamlines.

In gas-particle flow system, the similar flow field is only obtained if square of particle diameter is proportional to throat diameter. But by the particle sizing equations presented here the flow field never becomes similar by changing motor size. Fig.15 illustrates the scale effect on thrust performance. It can be seen that the Isp increases as high as the turnback angle, but is limited by particle impingement occurrence. Fig.16 shows an example of the computed variation of particle impingement location when the nozzle expansion ratio is fixed. The larger the nozzle length, the lower the allowable turnback angle. The allowable turnback angle becomes lower and finally becomes almost neutral as the motor scale becomes larger.
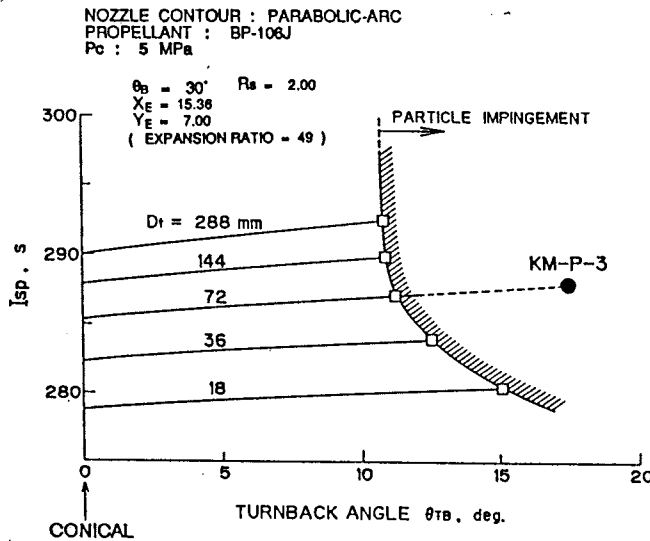

Fig. 15 Nozzle contour and motor scale
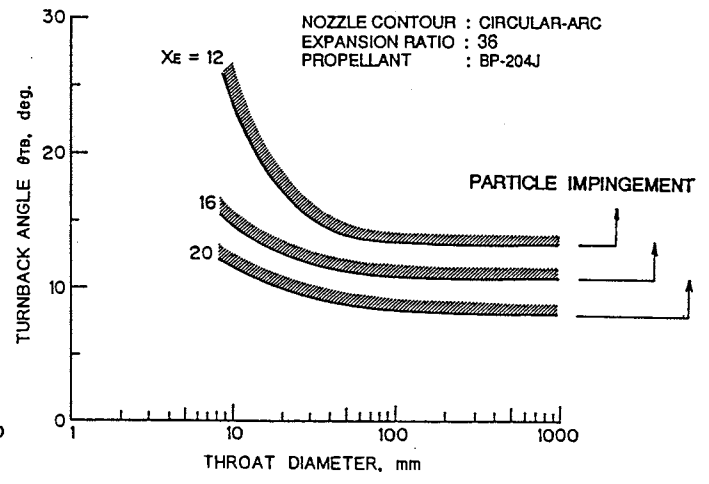effect on motor performance.

Fig. 16 Nozzle length and motor scale
effect on particle impingement.

6.CONCLUSION

The size distribution of alumina particles in the nozzle flow can well be characterized by log-normal distribution. The geometrical standard deviation is almost constant. D_{43} dependence on throat diameter is almost the same as that by the improved SPP. Numerical simulation by the improved ISAS' two-phase program well defined the two kinds of effective mean particle diameter, Dp_{ISP} to predict the motor performance and Dp_{IMP} to predict the particle impingement location.

The improved ISAS' program has achieved such a sufficient predictability as to be an effective nozzle contouring design tool. The nozzle contours of the upper stage motors of the new ISAS launch vehicle M-V are being designed to be optimum by employing this new designing scheme.

Reference

1) Doi, T., "Gas-Particle Nozzle Flows and Optimum Nozzle Shape," ISAS Report No.596, 1981.
2) Henderson, C. B., "Drag coefficients of Spheres in Continuum and Rarefied Flows," AIAA J., Vol.14, No.6, 1976.
3) Bartlett, R.W. and Delaney, L.J., "Effect of Liquid Surface Tension on Maximum Particle Size in Two-Phase Nozzle Flow," Pyrodynamics, Vol.4, 1966.
4) Hermsen, R.W., "Aluminum Oxide Particle Size for Solid Rocket Motor Performance Prediction," J. Spacecraft, Vol.18, No.6, 1981.
5) Ikeda, H., Tokudome, S., Tanno, H and Kohno, M., "Specific Impulse Prediction of Solid-Propellant Upper Stage Motors,"(in Japanese) Proc. of Symposium on Space Transportation, ISAS, 1989.
6) Kohno, M., Ikeda, H. and Yamamoto, Y., "Erosion Characteristics of Nozzle Throat Graphites in Solid Rocket Motors,"(in Japanese) Proc. of 32th Symposium on Space Science and Technology, Tokyo, 1988.
7) Ketner, D.M., and Hess, K.S., "Particle Impingement Erosion," AIAA-79-1250, 1979.
8) Danes, W.L. and Boyd, D.L., "Nozzle Contour Optimization for Solid-propellant Rocket Motors," AIAA-77-944, 1977.
9) Daines, W.L., Boardman, T.A., Lund, R.K. and Abel, R., "Effect of Aluminum Oxide Impingement on Specific Impulse of Solid Propellant Rocket Motors," AIAA-75-1277, 1975.